

# A simulation study on photoacoustic signals from red blood cells

Ratan K. Saha and Michael C. Kolios<sup>a)</sup>

Department of Physics, Ryerson University, 350 Victoria Street, Toronto, Ontario, M5B2K3 Canada

(Received 22 November 2010; revised 2 March 2011; accepted 3 March 2011)

A two dimensional simulation study was performed to investigate the photoacoustic signal properties of non-aggregated and aggregated erythrocytes. Spatial distributions of non-aggregated blood samples were generated by employing a Monte Carlo method and aggregated blood samples were simulated using a hexagonal packing scheme. For the non-aggregating case photoacoustic signals demonstrated a monotonic rise with hematocrit. For the aggregating case it was found that spectral (<20 MHz) intensity increased (11 dB at 15.6 MHz) when the aggregate size increased. This study strongly suggests that the assessment of erythrocyte aggregation level in human blood might be possible by using a photoacoustic spectroscopic method. © 2011 Acoustical Society of America. [DOI: 10.1121/1.3570946]

PACS number(s): 43.35.Ud, 43.80.Cs [CCC]

Pages: 2935–2943

## I. INTRODUCTION

Photoacoustic (PA) imaging is an active area of biomedical imaging research, that has attracted a lot of attention in the past few years.<sup>1</sup> In PA imaging, tissues are generally irradiated by a short-pulsed laser. Tissues absorb energy from the incident radiation, become heated, undergo thermoelastic expansions and subsequently emit pressure waves. Essentially, the optical and thermoelastic properties of a tissue are probed by detecting pressure waves using ultrasonic technologies after illumination by a laser radiation. There are two advantages associated with this modality. Images can be generated with better contrast than conventional ultrasound images and also PA imaging can image deeper tissues compared to that of conventional optical imaging modalities (e.g., confocal microscopy, two-photon microscopy etc.) with ultrasonic resolution. Strong contrast arises due to large differences of the light absorption properties of different tissues and detection of pressure waves in the receiving end allows to image deeper tissue regions. In recent years, exquisite images of the human and small animal vasculature have been produced by exploiting the large optical absorption of oxygenated and de-oxygenated blood at the relevant optical wavelengths.<sup>1</sup>

Moreover, estimates of tissue oxygenation can be made by the appropriate choice of the laser wavelength. The PA flowmetry methods have also been used to detect circulating melanoma cells in human blood and lymph nodes.<sup>2</sup> In another study, the PA technique along with the conventional ultrasound imaging have been implemented to detect and stage deep vein thrombosis.<sup>3</sup> In addition to that, PA signals from individual red blood cells (RBCs) has been detected using very high ultrasound frequencies.<sup>4</sup> However, the potential of PA imaging has never been employed to study the aggregation of red blood cells in human blood. While RBC aggregation in human blood is a normal phenomenon, hyper-aggregation is a pathological state. It is associated

with a wide range of pathological conditions, such as, acute myocardial infarction, cerebral ischemia, diabetes, and sickle cell disease.<sup>5–7</sup> It occurs due to the presence of large plasma proteins or macromolecules (e.g., fibrinogen) in blood in abnormal levels<sup>8</sup> and can lead to various cardiovascular and circulatory disorders.<sup>9</sup>

RBC aggregation is indirectly evaluated for clinical purposes through erythrocyte sedimentation rate (ESR) but this technique is poorly correlated with the RBC aggregation.<sup>10</sup> More accurate estimation of RBC aggregation can be made using light scattering techniques [e.g., laser-assisted optical rotation cell analyzer (LORCA)].<sup>10</sup> However, these are *in vitro* techniques and cannot be used for *in vivo* assessment of RBC aggregation. To achieve this various imaging and characterizing methods have been explored. For example, spectral domain Doppler optical coherence tomography technique has been used to measure RBC aggregation.<sup>11</sup> It was shown that variance of Doppler frequency spectrum was capable to differentiate non-aggregating and aggregating RBCs at hematocrits between 30% and 55% flowing at a shear rate of 40–60 s<sup>-1</sup>. In another investigation, X-ray phase contrast imaging modality has been used to examine the effects of RBC aggregation on speckles.<sup>12</sup> The size and contrast of speckles were found to be varied with the degree of RBC aggregation. So far a great deal of effort has also been put into developing ultrasound backscattering techniques as a noninvasive tool to monitor the level of RBC aggregation.<sup>13,14</sup> The aggregation mechanism essentially alters spatial organization of the cells which in turn produces large changes in ultrasound backscatter. Thus, it is intuitively expected that it might be possible to evaluate aggregation level by measuring pressure waves around the diagnostic ultrasound frequency range generated due to the absorption of light.

The aim of the paper is to illustrate the potential of using a PA method to characterize the level of aggregation of erythrocytes in human blood. The PA signals from a collection of red blood cells approximated as homogeneous spheres distributed in two dimensional space under non-aggregating and aggregating conditions were simulated by

<sup>a)</sup>Author to whom correspondence should be addressed. Electronic mail: mkolios@ryerson.ca

extending a theoretical model involving a frequency domain approach previously developed by Diebold *et al.*<sup>15</sup> that calculates the PA field generated by a spherical source exposed to a delta function laser (and thus heating) pulse. Spatial distributions of non-overlapping RBCs mimicking non-aggregated blood samples were generated by employing a Monte Carlo method known as the random sequential adsorption (RSA) technique. RBCs were packed following a hexagonal packing scheme to form a compact aggregate. Such an aggregate was repeated and randomly placed within the region of interest (abbreviated as ROI hereafter and refers to the region illuminated by the optical radiation) to simulate non-overlapping, isotropic, and identical RBC clusters representing an aggregated blood sample. This is a very simple and fast method to generate clusters. This approach has been successfully used in modeling ultrasound backscatter.<sup>16</sup> The mean radius of gyration of clusters for each aggregation level was computed to indicate effective cluster size. The PA signal properties such as signal envelope statistics and frequency dependent power spectra were investigated for these two types of blood samples. Our results show that a PA method can be implemented in practice to assess the level of red blood cell aggregation non-invasively.

The paper is organized as follows: In Sec. II we discuss the theoretical model and in Sec. III the computer simulation methods are described. The simulation results are presented in Sec. IV. Finally, Sec. V contains discussion of our results and conclusions are summarized in Sec. VI.

## II. THEORETICAL MODEL

The time dependent wave equation for the pressure generated by the absorption of optical radiation under the condition of thermal confinement (i.e., heat conduction remains zero before the pressure pulse is launched) can be written as<sup>15</sup>

$$\nabla^2 p - \frac{1}{v_s^2} \frac{\partial^2 p}{\partial t^2} = -\frac{\beta}{C_P} \frac{\partial H}{\partial t}, \quad (1)$$

where  $\beta$  is the isobaric thermal expansion coefficient,  $C_P$  is the heat capacity per unit mass, and  $v_s$  is the speed of sound in the illuminated region. Here,  $H$  is the thermal energy deposited by the optical radiation per unit time and volume.

If the optical radiation with intensity  $I_0$  propagates along the  $x$  axis and varies sinusoidally with time, the heating function can be expressed as,  $H(x, t) = \mu I_0 e^{-i\omega t}$ . Here,  $\mu$  is the optical absorption coefficient of the illuminated medium and  $\omega$  is the modulation frequency of the optical beam. For such a heating function the steady state pressure field will also vary sinusoidally and thus Eq. (1) reduces to the following time independent form,<sup>15</sup>

$$\nabla^2 p + k^2 p = \begin{cases} \frac{i\omega\mu\beta I_0}{C_P} & \text{inside the absorber,} \\ 0 & \text{outside the absorber,} \end{cases} \quad (2)$$

where  $k$  is the wave number of the pressure wave. This is an inhomogeneous partial differential equation. It is possible to obtain analytical solutions of Eq. (2) for some simple

geometries (e.g., layer, cylinder, sphere etc.) using the appropriate boundary conditions, namely continuity of pressure and the normal component of particle velocity. The PA pressure for uniform illumination of a spherical absorber at a distance  $r$  in the surrounding medium can be found as<sup>15</sup>

$$p_f^{\text{single}}(\hat{q}) = \frac{i\mu\beta I_0 v_s a}{C_P(r/a)} \times \frac{[\sin \hat{q} - \hat{q} \cos \hat{q}] e^{ik_f(r-a)}}{\hat{q}^2 [(1-\hat{\rho})(\sin \hat{q}/\hat{q}) - \cos \hat{q} + i\hat{\rho}\hat{v} \sin \hat{q}]}, \quad (3)$$

where the dimensionless frequency  $\hat{q}$  is defined as  $\hat{q} = \omega a / v_s$  and  $a$  is the radius of the absorbing sphere. Similarly, the dimensionless quantities  $\hat{\rho} = \rho_s / \rho_f$  and  $\hat{v} = v_s / v_f$  represent the ratios of density and speed of sound, respectively. The subscripts  $s$  and  $f$  are used to indicate properties of the absorber and the surrounding fluid medium, respectively. Here,  $k_f$  is the wave number in the fluid medium for the pressure wave with frequency  $\omega$  and is given by  $k_f = \omega / v_f$ . Further, the superscript single in Eq. (3) signifies that only one PA source is considered. The expression of time dependent PA pressure can readily be derived by taking the Fourier transformation of Eq. (3) and for a delta function heating pulse it becomes<sup>15</sup>

$$p_f^{\text{single}}(\hat{\tau}) = \frac{i\mu\beta F v_s^2}{2\pi C_P(r/a)} \int_{-\infty}^{\infty} d\hat{q} \times \frac{[\sin \hat{q} - \hat{q} \cos \hat{q}]}{\hat{q}^2 [(1-\hat{\rho})(\sin \hat{q}/\hat{q}) - \cos \hat{q} + i\hat{\rho}\hat{v} \sin \hat{q}]} e^{-i\hat{q}\hat{\tau}}, \quad (4)$$

where the pressure field has been presented as a function of dimensionless retarded time  $\hat{\tau}$  from the edge of the sphere and it is defined as  $\hat{\tau} = (v_s/a)[t - (r-a)/v_f]$ . Here,  $F$  indicates the optical radiation fluence.

In many situations related to light scattering and ultrasound scattering by random media, scattered fields have been expressed as a superposition of spherical waves generated by the scatterers. This is essentially based on the single particle approach and works well for a sparse medium. This approach has been used extensively in many fields to explain experimental results.<sup>17-19</sup> The single particle approach has been employed here. It was also assumed that the absorbers were illuminated by a light with constant intensity irrespective of their spatial positions. That means all double and multiple scatterings of light beam were assumed to be negligible. Moreover, acoustic waves generated by a light absorbing particle did not interact with other particles in the medium. With these assumptions, the PA pressure field generated by a collection of absorbing spheres can be written as a linear superposition of spherical waves emitted by the individual sources as

$$p_f^{\text{ensemble}}(\hat{q}) = \frac{i\mu\beta I_0 v_s a^2}{C_P} \times \frac{[\sin \hat{q} - \hat{q} \cos \hat{q}]}{\hat{q}^2 [(1-\hat{\rho})(\sin \hat{q}/\hat{q}) - \cos \hat{q} + i\hat{\rho}\hat{v} \sin \hat{q}]} \times \sum_{n=1}^N \frac{e^{ik_f(|\mathbf{r}-\mathbf{r}_n|-a)}}{|\mathbf{r}-\mathbf{r}_n|}. \quad (5)$$

The summation term in the above equation accounts for the interference of pressure waves generated by many (as denoted by the superscript ensemble) spheres distributed in space. Here,  $\mathbf{r}_n$  represents the position vector of the  $n$ th particle and the ROI contains  $N$  PA sources. If the observation distance  $r$  is large compared to the size of the ROI, the terms,  $k_f|\mathbf{r} - \mathbf{r}_n|$  in the numerator and  $|\mathbf{r} - \mathbf{r}_n|$  in the denominator of Eq. (5) can be approximated as,  $k_f|\mathbf{r} - \mathbf{r}_n| \rightarrow k_f r - \mathbf{k}_f \cdot \mathbf{r}_n$  and  $|\mathbf{r} - \mathbf{r}_n| \rightarrow r$ , respectively.<sup>19</sup> Here,  $\mathbf{k}_f$  defines the direction of observation. Therefore, Eq. (5) reduces to

$$p_f^{\text{ensemble}}(\hat{q}) \approx \frac{i\mu\beta I_0 v_s a}{C_p(r/a)} \times \frac{[\sin \hat{q} - \hat{q} \cos \hat{q}] e^{ik_f(r-a)}}{\hat{q}^2[(1-\hat{\rho})(\sin \hat{q}/\hat{q}) - \cos \hat{q} + i\hat{\rho}\hat{v} \sin \hat{q}]} \times \sum_{n=1}^N e^{-i\mathbf{k}_f \cdot \mathbf{r}_n}. \quad (6)$$

The time dependent pressure field can be derived as

$$p_f^{\text{ensemble}}(\hat{\tau}) \approx \frac{i\mu\beta F v_s^2}{2\pi C_p(r/a)} \int_{-\infty}^{\infty} d\hat{q} \times \frac{[\sin \hat{q} - \hat{q} \cos \hat{q}]}{\hat{q}^2[(1-\hat{\rho})(\sin \hat{q}/\hat{q}) - \cos \hat{q} + i\hat{\rho}\hat{v} \sin \hat{q}]} \times e^{-i\hat{q}\hat{\tau}} \sum_{n=1}^N e^{-i\mathbf{k}_f \cdot \mathbf{r}_n}. \quad (7)$$

In this work the above integration has been evaluated numerically to compute pressure fields at a large distance from the center of the ROI at various non-aggregating and aggregating conditions of red blood cells.

### III. SIMULATION METHODS

#### A. Simulation parameters

A 2D simulation study was carried out to examine the PA signal properties of non-aggregated and aggregated blood samples. 2D simulations are computationally less intensive than that of 3D and are capable in generating physically meaningful results.<sup>20,21</sup> It is also easier to visualize and distinguish different cluster geometries in 2D. The size of the region of interest was chosen as  $200 \times 200 \mu\text{m}^2$  and could be thought as a 2D slice of a blood sample. The RBCs in a blood sample could be assumed to be the dominant absorbers of the incident optical radiation as well as sources of PA emissions. In many experiments the wavelength of the laser beam has been tuned to the most optimal optical absorption of erythrocytes.<sup>3</sup> Also, RBCs are much more numerous than other blood cells ( $\approx 98\%$  of blood cells are RBCs). Thus, the contributions from white blood cells and platelets in PA signals from bloods were neglected in this study. In the present study we also approximated RBCs as homogeneous spheres with a volume  $87 \mu\text{m}^3$  and radius  $a = 2.75 \mu\text{m}$  for each cell. The density and speed of sound within RBCs were taken as  $\rho_s = 1092 \text{ kg/m}^3$  and  $v_s = 1639 \text{ m/s}$ , respectively.<sup>22</sup> The numerical values of the same quantities of the surrounding medium (blood plasma) were chosen as  $\rho_f = 1005 \text{ kg/m}^3$  and  $v_f = 1498 \text{ m/s}$ .<sup>22</sup> The cells were

TABLE I. Physical constants and parameters used in simulations.

ROI	$200 \times 200 \mu\text{m}^2$
$a$	$2.75 \mu\text{m}$
$\rho_s$	$1092 \text{ kg/m}^3$
$v_s$	$1639 \text{ m/s}$
$\rho_f$	$1005 \text{ kg/m}^3$
$v_f$	$1498 \text{ m/s}$
$\beta$	$1 \text{ K}^{-1}$
$C_p$	$1 \text{ J kg}^{-1}\text{K}^{-1}$
$\mu$	$1 \text{ m}^{-1}$
$F$	$1 \text{ Jm}^{-2}$

hypothesized to be in the similar bio-physical and bio-chemical conditions, which in turn allowed to consider the numerical values of the physical parameters ( $\beta$ ,  $C_p$ , and  $\mu$ ) to be same for all cells. It was further approximated that the cells were illuminated by a light with constant intensity irrespective of their spatial locations. Therefore, these parameters ( $\beta$ ,  $C_p$ ,  $\mu$ , and  $F$ ) were treated as constants and were taken as equal to unity in this study. Table I summarizes the numerical values that were used to compute Eq. (7). The RBCs were positioned in the region of interest for non-aggregating and aggregating conditions to simulate 2D tissue realizations. For each case 250 frames representing possible tissue configurations were simulated to generate 250 PA radio frequency (RF) lines by computing Eq. (7). The integration in Eq. (7) at each time point was evaluated numerically by employing the trapezoidal rule and the computed PA pressure was a complex quantity. The PA RF line was obtained from the real parts of PA pressure time series data and signal envelope was determined from the corresponding magnitudes. The computer codes written in C were executed in a remote computer cluster. Post processing of data were performed in MATLAB R2009b.

#### B. Simulation of non-aggregated red blood cells

A blood tissue realization of non-aggregated RBCs was generated by using a Monte Carlo method known as the RSA technique.<sup>23</sup> In this method the coordinates of a RBC were chosen randomly with the restriction that it would not overlap with the existing particles under the periodic boundary conditions, although they might touch. In other words coordinates of a RBC were proposed randomly and accepted if it satisfied the non-overlapping conditions (i.e., cells must be separated by a distance equal to or more than their diameters) with other cells. If there was a overlap, the trial move was canceled and a new move was initiated. In this way the coordinates of a RBC were generated. This step was repeated until coordinates of all red blood cells at a particular hematocrit were assigned. The term hematocrit is defined as the fractional volume occupied by the cells. However, in this 2D simulation study it was obtained from the ratio of area occupied by the cells to the total area of the ROI. Once the spatial positioning of RBCs was completed, Eq. (7) was then computed to obtain the PA RF line and signal envelope for that spatial organization of cells. The average signal amplitude was evaluated subsequently from that envelope data set.

TABLE II. RBC aggregation parameters associated with various simulated tissue samples.

Non-aggregated blood	H	0.02–0.50
	N	34–842
	$R_g$	2.13 $\mu\text{m}$
Aggregated blood	H	0.40
	N	674
	Cl	54.82–11.78
	$N_{Cl}$	11.83–57.10
	$N_{nag}$	24.41–1.77
	$R_g$	7.57–15.39 $\mu\text{m}$

This procedure was repeated for 250 RF lines generated from 250 different tissue realizations. Finally, the mean [indicated by  $\langle \text{PA signal amplitude} \rangle$ , in the Figs. 2(f) and 3(f)] and standard deviation were determined from the 250 numerical values for each hematocrit. The signal envelope histogram was also obtained from the 250 RF lines for each hematocrit and fitted with a Rayleigh distribution function [see Eq. (A1) of the Appendix]. The best fitted Rayleigh distribution curve was obtained by optimizing the theoretical model and the simulated histogram. Essentially, at each hematocrit the  $\sigma$  value was estimated at first from the first order moment of envelope data set as given by Eq. (A2). This estimated value was then provided to a MATLAB function known as the ‘fminsearch’ as a guess for the fitting parameter and that function carried out the optimization (it uses the Nelder–Mead simplex algorithm<sup>24</sup>) to generate the best fitted curve. In this work PA signal characteristics of blood samples with non-aggregated RBCs were studied at various hematocrits,  $H = 0.02\text{--}0.50$ . The corresponding numbers of particles were counted to be 34–842 as displayed in Table II.

### C. Simulation of aggregated red blood cells

A blood tissue configuration of aggregated RBCs can be generated in various ways. For example, Savery *et al.*<sup>20</sup> empirically modeled the cellular pair interaction energy as a combination of steric and attractive potentials and then applied the Monte Carlo technique to evolve the system over a large number of iterations to generate two dimensional distributions of aggregated RBCs. In another Monte Carlo study,<sup>25</sup> cells were allowed to interact via a Morse type of potential to form three dimensional distributions of aggregated RBCs. However, both the methods are computationally intensive and also do not always generate compact RBC clusters; only random loose pack (RLP) configurations only be achieved. In two dimensions RLP can provide 54%–55% packing density of cells whereas it is about 60% in three dimensions.<sup>23</sup> Thus, they are not capable to provide compact clusters. However, to generate tightly packed RBC clusters one can rely on regular packing schemes. For instance, in two dimensions a packing density of circles of nearly 90% can be attained through a hexagonal packing scheme.<sup>26</sup> In this study this packing scheme was followed to arrange circles representing RBCs in order to form an aggregate. This cluster was repeated and placed randomly within the ROI to generate an aggregated blood sample. Note that this

is a very fast method because cells are placed at fixed locations in an aggregate and also capable to form compact clusters.

A flow chart diagram illustrating the steps used to generate the spatial distribution of the RBCs is shown in Fig. 1. At first the total number of cells were obtained by fixing the hematocrit and the size of the ROI. In this study, the PA signal properties of blood samples at 40% hematocrit and at different clustering or aggregating conditions were examined. A hematocrit level of 40% was chosen because it is close to the normal level of hematocrit ( $\approx 45\%$ ) in normal human blood.<sup>19</sup> The next step was to find the spatial positions of randomly distributed, well separated, isotropic clusters of identical size within the ROI under periodic boundary conditions using the same RSA algorithm. The number of clusters also fixed the number of cells, that could be attached per cluster. The number of cells per cluster was determined by dividing the total number of cells by the number of clusters and truncating that numerical value to the nearest lower integer value. That number of cells were positioned using the hexagonal packing arrangement for each cluster.

To do this initially a large number of circles representing RBCs were stacked in a rectangular area following the hexagonal packing scheme.<sup>26</sup> After that coordinates of the center of a circle located at the central region of that rectangular area was chosen. Coordinates of the centers of other circles were recorded according to their distances with respect to that reference point to form a lookup table. The next step was to take the coordinates of the required number of circles attached to a cluster from this lookup table and place them with respect to the center of a cluster. Note that the lookup table provided the coordinates of the circles with respect to the cluster center. However, the coordinates of those circles with respect to the origin of the ROI are required for the computation of Eq. (7) and that could easily be obtained by summing coordinates (available from the lookup table) of those circles and that of the cluster center. Similarly the coordinates of the circles associated with other clusters were taken from the lookup table and they were transformed into the coordinate system of the ROI. The circles, which did not belong to any cluster were positioned within the ROI under non-overlapping conditions with other circles. In this way spatial distributions of non-overlapping, isotropic and identical clusters containing non-overlapping cells were generated. Furthermore, for each aggregating condition the mean radius of gyration of clusters was computed to quantify the mean cluster size. The radius of gyration of a cluster was determined by using the square of the distances of the cells from the center of the cluster such as

$$R_g = \left( \frac{3}{5} a^2 + \frac{1}{n_c} \sum_{j=1}^{n_c} r_j^2 \right)^{1/2}, \quad (8)$$

where  $n_c$  is the number of cells attached to a cluster and  $r_j$  is the distance of the center of the  $j$ th cell from the cluster center. The numerical values of  $R_g$  were obtained for all clusters associated with a tissue realization and the average value was computed subsequently. Further, the non-aggregated

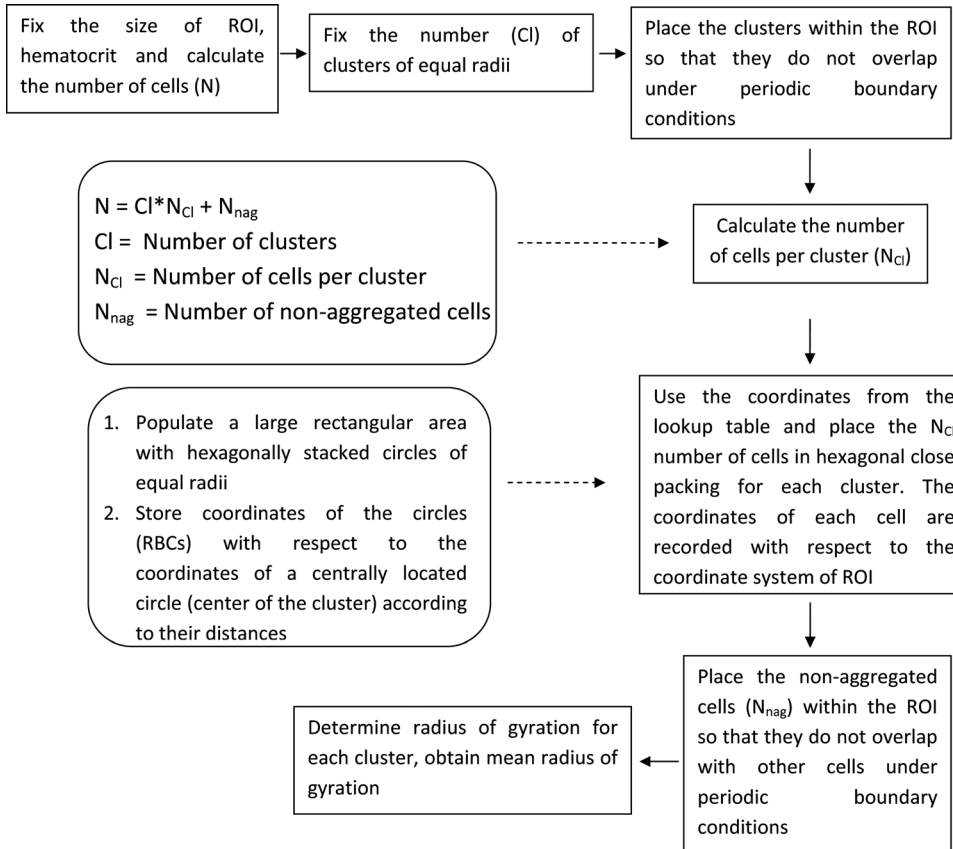


FIG. 1. Flow chart diagram demonstrating the method to generate the spatial distribution of red blood cells in clusters that mimic an aggregated blood tissue sample.

RBCs were not considered in order to estimate the mean radius of gyration of clusters.

Table II displays the numerical values of different quantities characterizing aggregated blood samples examined in this study. For instance, the mean number of clusters varied between  $\approx 54.82$  and  $11.78$  from the lowest to the highest clustering condition. The average number of particles associated with a cluster lied in the range from  $11.83$  to  $57.10$  and for all samples very few numbers ( $< 4\%$ ) of cells were not part of aggregates. The lowest value of mean radius of gyration of clusters was estimated to be  $7.57 \mu\text{m}$  and that of the highest aggregation was  $15.39 \mu\text{m}$ .

#### IV. SIMULATION RESULTS

Figure 2(a) demonstrates two dimensional spatial organization of red blood cells mimicking a tissue realization with non-aggregated RBCs at  $H=0.40$ . Each circle represents a RBC. Figure 2(b) shows a representative PA RF line computed by using Eq. (7) at the same hematocrit level. The corresponding envelope histogram, generated over 250 RF lines, is presented in Fig. 2(c). It also shows that the Rayleigh distribution [see Eq. (A1) of the Appendix] provides good fit to the envelope histogram. Variations of PA mean power spectra at several hematocrits are shown in Fig. 2(d) over a wide range of frequencies (MHz to GHz). For each hematocrit the mean power spectrum was obtained from 250 RF lines. The spectral intensity increased as the number of cells within the region of interest (hematocrit) increased.

The same plots of Fig. 2(d) are shown on a log–log scale in Fig. 2(e). Figure 2(f) illustrates how the mean ( $\pm 1$  standard deviation) of PA signal amplitudes varies with hematocrit. A monotonic increase of PA signal is observed with increased concentration of red blood cells. Karpiouk *et al.*<sup>3</sup> also experimentally obtained a similar variation of measured PA signals with hematocrit.

A representative diagram of aggregated red blood cells at 40% hematocrit forming non-overlapping, isotropic, and identical clusters with mean radius of gyration,  $R_g = 12.24 \mu\text{m}$  is shown in Fig. 3(a). In this figure small circles represent individual RBCs and big circles outline the cluster boundaries. The effects of periodic boundary conditions can also be seen in this figure (if a portion of a cluster crossed a boundary wall then that portion appeared in the opposite side). Some cells not belonging to any cluster occupy random positions within the ROI. A typical PA signal for this sample is displayed in Fig. 3(b). The corresponding envelope histogram of that sample is shown in Fig. 3(c). Although the envelope histogram followed the Rayleigh distribution, however, the width of the histogram increased compared to that of non-aggregated blood. The mean power spectra for a series of aggregation levels are shown in Fig. 3(d) for frequencies up to 100 MHz. Frequency spectra beyond 100 MHz were complex and thus have been omitted in Fig. 3(d) for clarity. It can be seen that first frequency minimum appeared at lower frequency as the cluster size increased. This figure also shows that the spectral intensity in the low frequency range increased significantly as the mean size of clusters

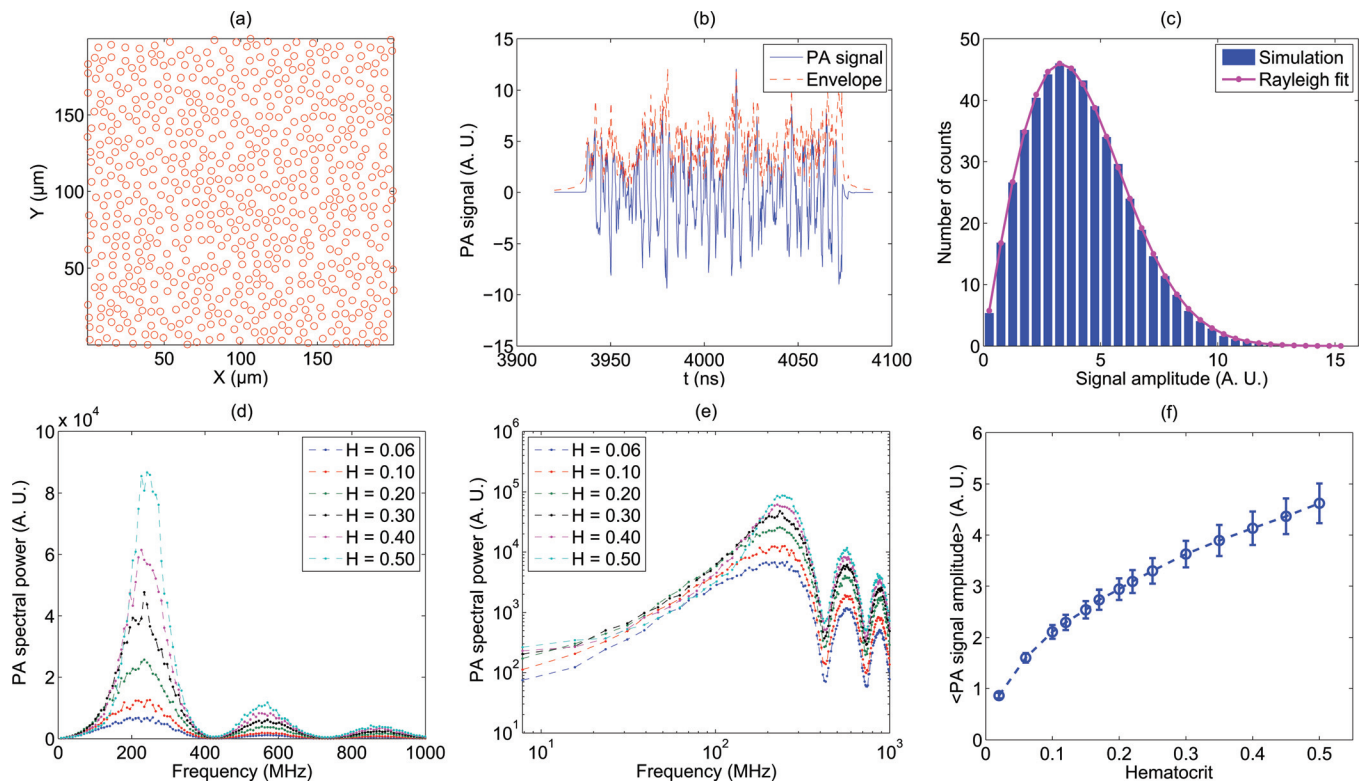


FIG. 2. (Color online) (a): An arrangement of randomly located red blood cells (represented by circles) for a hematocrit of  $H = 0.40$ . (b) A representative plot of a PA signal in arbitrary units (A.U.). (c) Signal envelope histogram (250 RF lines were used). (d) Plots of PA power spectra for blood samples at different hematocrits. (e) Same as (d) but plotted on a log–log scale. (f) Variation of mean ( $\pm 1$  SD) of the PA signal amplitudes with hematocrit.

increased compared to the non-aggregating case. For example, at 15.6 MHz for aggregating conditions with  $R_g = 9.97$  and  $15.39 \mu\text{m}$  there are  $\approx 8$  and 11 dB enhancements of PA spectral intensity compared to that of non-aggregated blood, respectively. The corresponding values were 9 and 16 dB at 23.4 MHz. Essentially, the alteration of the spatial organization (non-aggregation to aggregation) of cells could cause great reduction in the destructive interference of the PA waves (originating from the cells) in the lower frequency range. This resulted in significant enhancement of spectral intensity in this frequency range, which is linked to the aggregate size. The large increase in spectral intensity clearly suggests that non-aggregated and aggregated blood samples could easily be distinguished by using PA spectroscopy. The positions of first frequency minimum occurred at nearly 55 and 40 MHz, respectively for two aggregated blood samples whereas it was about 420 MHz for the non-aggregated blood sample. Thus, position of first frequency minimum also showed great sensitivity to the RBC cluster size. The same plots of Fig. 3(d) are presented in Fig. 3(e) on a log–log scale over a large frequency range. It shows that the spectral intensity curves follow complicated patterns after first minimum and are not straightforward to interpret. A plot of the PA signal amplitude with cluster size [expressed in terms of radius of gyration ( $R_g$ )] is shown in Fig. 3(f) and it increased as the mean aggregate size increased. For instance,  $\approx 34\%$  enhancement of the mean signal amplitude was computed for the blood sample with the largest cluster size when compared to that of non-aggregated blood sample.

## V. DISCUSSION

A theoretical formulation based on the single particle approach is presented here to describe the PA pressure field generated by a collection of erythrocytes. The resultant PA field in this formalism has been written as a summation of spherical waves emitted by the individual cells. The theoretical framework assumes that the effects of double and multiple scattering of light waves are negligible. Therefore, this theory would require further development for situations when this assumption cannot be made. Moreover, optical absorption coefficients for all cells were fixed to a constant value assuming that the cells were in the same oxygenation state. In general, this approximation is not valid because oxygen level may vary for different cells. However, if we chose a wavelength (e.g.,  $\approx 584$  or  $800$  nm, the isosbestic point<sup>27,28</sup>) for which oxygenated and deoxygenated red blood cells have similar absorption coefficients and then cell oxygenation state does not play a role in the PA signals. For such a wavelength this model will be applicable without any modification.

The simulated PA signal amplitude for non-aggregated RBCs demonstrated a monotonic increase with hematocrit [Fig. 2(f)] and that was also observed in an experimental study.<sup>3</sup> It may be argued that the signal strength increases as the concentration of particles increases. Higher concentration means more PA sources and that results in stronger PA signal. However, in ultrasound imaging, ultrasound backscatter coefficient for non-aggregated RBCs exhibits a non-linear behavior with hematocrit. The theoretical backscatter

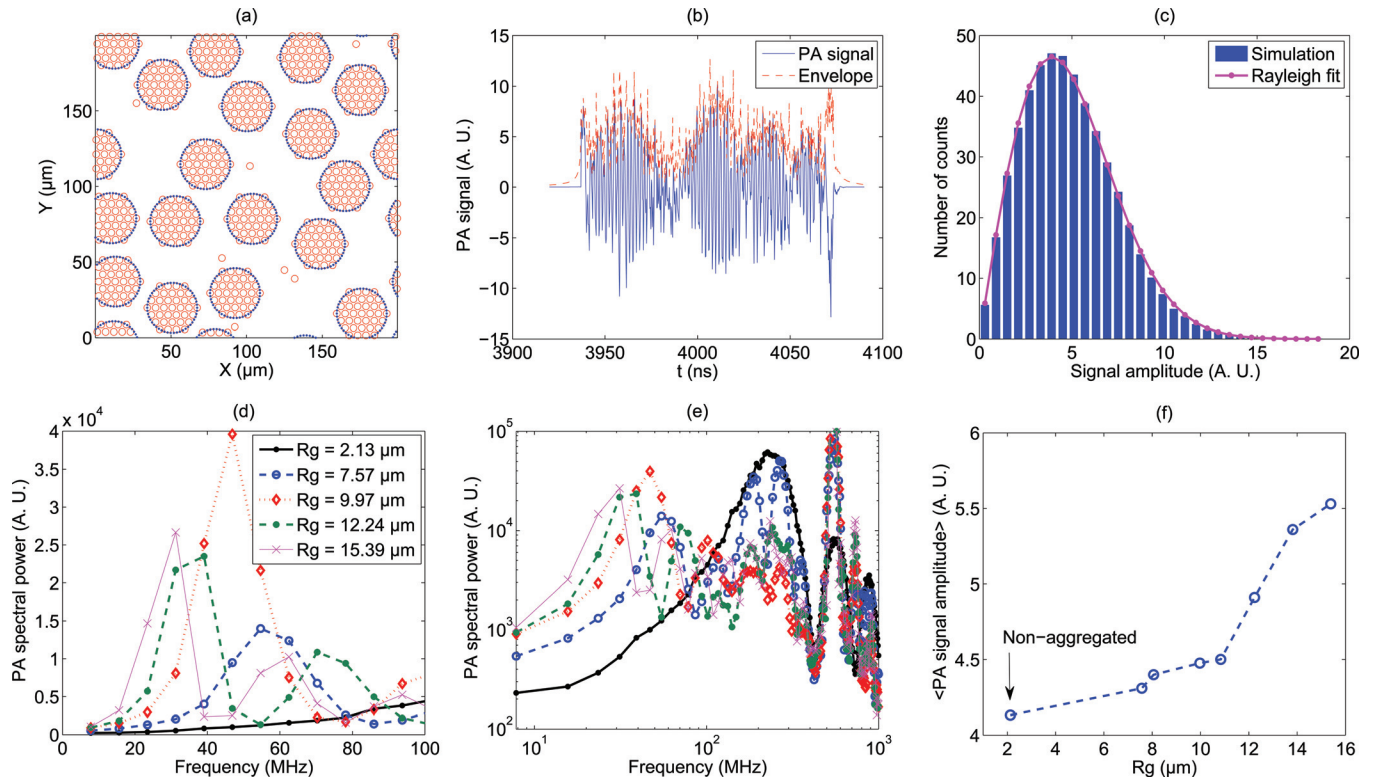


FIG. 3. (Color online) (a): An arrangement of randomly located RBC clusters for  $H = 0.40$ . Small circles are individual RBCs and big circles show the cluster boundaries (with mean radius of gyration,  $R_g = 12.24 \mu\text{m}$ ). (b) A representative plot of a PA signal. (c) Signal envelope histogram (250 RF lines were used). (d) Plots of PA power spectra starting from non-aggregated blood sample with  $R_g = 2.13 \mu\text{m}$  to other samples with different cluster sizes but at fixed hematocrit of 40%. Cluster size increased as  $R_g$  increased. (e) Same as (d) but plotted on a log-log scale. In this figure the same sequence of (d) has been used to draw the curves associated with different aggregation levels. (f) Variation of mean PA signal amplitude with mean RBC cluster size (expressed in radius of gyration,  $R_g$ ).

coefficient, computed at 7.5 MHz, initially increases with hematocrit, reaches to its peak at nearly 13% hematocrit and then decreases as the hematocrit increases.<sup>19</sup> A similar pattern has also been observed experimentally.<sup>19</sup> At low cell concentration the backscatter coefficient increases with hematocrit because the backscatter intensities of individual RBCs add up in this case. But at higher RBC concentration, if the size of the scattering volume is much larger than wavelength, then a pair of RBCs can be found for which backscatter waves will interfere destructively and therefore the backscatter coefficient will drop with hematocrit.<sup>19</sup> It is clear that photoacoustic and ultrasound signal properties of RBCs are opposite in nature at higher concentration of cells. Further investigation is required to clarify such opposite trends in terms of interfering waves and concentrations of sources and scatterers. However, the finite bandwidth of an ultrasound pulse (and therefore limited range of frequencies of the scattered sound) is thought to play a significant role.

The model presented here has also been used to investigate how PA signal amplitude and the power spectrum would vary with the level of RBC aggregation. It was observed that the PA signal amplitude increased as the level of aggregation increased. Nevertheless, experimental confirmation of this finding is required as there are many other factors (such as effects of flow, intervening tissues, ultrasound transducer receiver bandwidth etc.) that may influence the sensitivity of the proposed technique. Once all these factors are included, then

the technique could be designed to measure RBC aggregation levels associated with a wide range of pathologies.

The simulation algorithm implemented here was capable to generate compact clusters. Only few cells were left in the non-aggregated state in the simulated tissue configurations mimicking aggregated blood samples. For example, for the highest clustering condition with  $R_g = 15.39 \mu\text{m}$ , 99.74% cells formed clusters and 0.26% cells remained in non-aggregated state. Also the mean packing density of cells in clusters was computed to be  $0.71 \pm 0.03$  from 250 tissue realizations. On the other hand in a configuration for the tissue sample with smallest clusters ( $R_g = 7.57 \mu\text{m}$ ), 96.37% cells attached to the clusters and 3.63% cells found to be non-aggregated cells. The corresponding mean packing density of cells in clusters was estimated to be  $0.59 \pm 0.02$  from the same numbers of tissue configurations. Further, this is a very fast method because cells occupy only some fixed locations within a cluster. For instance, the execution time to generate 50 PA RF lines from 50 different tissue configurations with the mean aggregate size,  $R_g = 15.39 \mu\text{m}$  was about 35 min in a remote computer cluster (Specification for each node- Operating System: Linux CentOS 5, RAM: 16 GB, Processor: Intel Xenon E5462 Quad Core 2.8 GHz).

An interesting point is to note that the samples were illuminated by a delta function heating pulse. Accordingly, the PA signals generated here contained a wide range of frequencies [MHz to GHz, Figs. 2(d) and 2(e) and Figs. 3(d)

and 2(e)]. For these signals the Rayleigh distribution provided quite accurate fittings to the simulated envelope histograms for both non-aggregated and aggregated blood samples. However, the same trend may not be observed in practise because a ultrasound transducer would modify the characteristics of the signals detected due to its frequency dependent sensitivity. Therefore, it would be of interest to investigate the bandwidth dependent signal histogram features particularly for aggregated blood samples. The bandwidth dependent spectral variations appeared in Figs. 3(d) and 3(e) due to spatial organization of cells suggest that the envelope histogram patterns might not be same for different receiving bandwidths. In that case the Rayleigh distribution might not be a suitable distribution to describe various histogram patterns. Some other more general distributions (such as the Nakagami, generalized gamma, homodyned K distributions) might be employed to fit the histograms.<sup>29–32</sup> In the context of ultrasound tissue characterization these distributions have been used extensively to model envelope histograms arising from different scattering conditions and provided useful information related to scatterer concentrations and their spatial organizations.<sup>29–32</sup>

## VI. CONCLUSIONS

The potential of using PA methods to assess the level of aggregation of red blood cells in human blood is discussed. For this purpose a 2D simulation study has been carried out with non-aggregated and aggregated blood samples. Spatial distributions of blood samples containing non-aggregated RBCs at different hematocrits were generated by using a Monte Carlo method known as the RSA technique. The red blood cells were packed by using hexagonal packing scheme to form a compact aggregate. Such an aggregate was repeated and randomly placed within the region of interest to simulate non-overlapping, isotropic, and identical RBC clusters mimicking an aggregated blood sample. PA signal properties involving signal envelope statistics and frequency power spectra were computed and subsequently examined for both types of blood samples. The use of PA method to evaluate the level of RBC aggregation in human blood and the simulation technique presented here to the best of our knowledge have never been discussed previously.

It was observed that the PA signal strength increased monotonically as the concentration of red blood cells increased. This is consistent with experimental findings for non-aggregated RBCs.<sup>3</sup> Moreover, envelope histograms followed the Rayleigh distribution for the entire hematocrits ranging from 0.02 to 0.50. It was found that the spectral intensity at 15.6 MHz increased about 11 dB for an aggregated blood sample with 40% hematocrit (and 15.39  $\mu\text{m}$  as the mean radius of gyration of clusters) compared to that of non-aggregated blood at the same hematocrit with 2.13  $\mu\text{m}$  as the mean radius of gyration. Similarly an enhancement of 16 dB was recorded at 23.4 MHz. These numerical values suggest that assessment of the RBC aggregation level in human blood using PA spectroscopy methods is feasible. The histograms of the envelope statistics in this case also followed the Rayleigh distributions and the  $\sigma$  parameter of that distribu-

tion increased as the cluster size increased (with the hematocrit remained constant at 40%). Future work would include extending the simulations to 3D systems and experimental validation of these findings.

## ACKNOWLEDGMENTS

This work was jointly supported by the Canadian Institutes of Health Research grant MOP-97959 and the Canada Research Chairs Program awarded to M. C. K. The computational facilities of the Shared Hierarchical Academic Research Computing Network (SHARCNET:www.sharcnet.ca) and Compute/Calcul Canada were used. We also acknowledge “Réseau Québécois de Calcul de Haute Performance” (RQCHP), where a part of the simulation work was performed. We also gratefully thank Dr. Min Rui, Dr. Sankar Narshimhan, Dr. Behrouz Soroushian (now at the University of Kansas) and Mr. Eno Hysi of Ryerson University for stimulating discussions and insightful questions.

## APPENDIX

The probability density function (PDF) of the Rayleigh distribution is given by

$$f(y) = \frac{y}{\sigma^2} \exp\left(-\frac{y^2}{2\sigma^2}\right), \quad (\text{A1})$$

where  $\sigma$  is the scale parameter and  $2\sigma^2$  provides the average intensity of the Rayleigh distribution.<sup>32</sup> If  $Y$  is a random variable with a Rayleigh PDF, then

$$\sigma = \frac{E(Y)}{1.253}, \quad (\text{A2})$$

where  $E$  is the expected-value operator.

<sup>1</sup>L. V. Wang, “Prospects of photoacoustic tomography,” *Med. Phys.* **35**, 5758–5767 (2008).

<sup>2</sup>R. M. Weight, P. S. Dale, and J. A. Viator, “Detection of circulating melanoma cells in human blood using photoacoustic flowmetry,” *Proceedings of the 31st Annual International Conference of the IEEE EMBS*, pp. 106–109 (2009).

<sup>3</sup>A. B. Karpouk, S. R. Aglyamov, S. Mallidi, J. Shah, W. G. Scott, J. M. Rubin, and S. Y. Emelianov, “Combined ultrasound and photoacoustic imaging to detect and stage deep vein thrombosis: Phantom and *ex vivo* studies,” *J. Biomed. Opt.* **13**(5), 1–8 (2008).

<sup>4</sup>M. Rui, W. Bost, E. Weiss, R. Lemor, and M. C. Kolios, “Photoacoustic Microscopy and Spectroscopy of Individual Red Blood Cells” in *Biomedical Optics, OSA Technical Digest (CD)* (Optical Society of America, 2010), paper BSuD93.

<sup>5</sup>H. J. Meiselman, “Red blood cell aggregation: 45 years being curious,” *Biorheology* **46**, 1–19 (2009).

<sup>6</sup>J. J. Bishop, A. S. Popel, M. Intaglietta, and P. C. Johnson, “Rheological effects of red blood cell aggregation in the venous network: A review of recent studies,” *Biorheology* **38**, 263–274 (2001).

<sup>7</sup>S. Kim, A. S. Popel, M. Intaglietta, and P. C. Johnson, “Aggregate formation of erythrocytes in postcapillary venules,” *Am. J. Physiol. Heart Circ. Physiol.* **288**, H584–H590 (2005).

<sup>8</sup>H. Bäumlér, B. Neu, E. Donath, and H. Kiesewetter, “Basic phenomena of red blood cell rouleaux formation,” *Biorheology* **36**, 439–442 (1999).

<sup>9</sup>A. Chabenel, M. H. Horellou, J. Conard, and M. M. Samama, “Red blood cell aggregability in patients with a history of leg vein thrombosis: influence of post-thrombotic treatments,” *Br. J. Haematol.* **88**, 174–179 (1994).

- <sup>10</sup>R. B. Ami, G. Barshtein, D. Zeltser, Y. Goldberg, I. Shapira, A. Roth, G. Keren, H. Miller, V. Prochorov, A. Eldor, S. Berliner, and S. Yedgar, "Parameters of red blood cell aggregation as correlates of the inflammatory state," *Am. J. Physiol. Heart Circ. Physiol.* **280**(5), H1982–H1988 (2001).
- <sup>11</sup>X. Xu, L. Yu, and Z. Chen, "Velocity variation assessment of red blood cell aggregation with spectral domain Doppler optical coherence tomography," *Ann. Biomed. Eng.* **38**, 3210–3217 (2010).
- <sup>12</sup>S. J. Lee, H. Ha, and K.-H. Nam, "Measurement of red blood cell aggregation using X-ray phase contrast imaging," *Opt. Express* **18**, 26052–26061 (2010).
- <sup>13</sup>F. T. H. Yu and G. Cloutier, "Experimental ultrasound characterization of red blood cell aggregation using the structure factor size estimator (SFSE)," *J. Acoust. Soc. Am.* **122**, 645–656 (2007).
- <sup>14</sup>E. Franceschini, F. T. H. Yu, F. Destrempes, and G. Cloutier, "Ultrasound characterization of red blood cell aggregation with intervening attenuating tissue mimicking phantoms using structure factor size and attenuation estimator," *J. Acoust. Soc. Am.* **127**, 1104–1115 (2010).
- <sup>15</sup>G. J. Diebold, "Photoacoustic monopole radiation: Waves from objects with symmetry in one, two and three dimensions," in *Photoacoustic Imaging and Spectroscopy*, edited by L. V. Wong (Taylor & Francis Group, LLC, London, 2009), Chap. 1, pp. 3–17.
- <sup>16</sup>R. K. Saha, E. Franceschini, and G. Cloutier, "Assessment of accuracy of the structure-factor-size-estimator method in determining red blood cell aggregate size from ultrasound spectral backscatter coefficient," *J. Acoust. Soc. Am.* **129**, 2269–2277 (2011).
- <sup>17</sup>A. Ishimaru, *Wave Propagation and Scattering in Random Media* (Academic, New York, 1978), Chap. 4, pp. 69–92.
- <sup>18</sup>M. F. Insana, R. F. Wagner, D. G. Brown, and T. J. Hall, "Describing small-scale structure in random media using pulse-echo ultrasound," *J. Acoust. Soc. Am.* **87**, 179–192 (1990).
- <sup>19</sup>K. K. Shung and G. A. Thieme, *Ultrasound Scattering in Biological Tissues* (CRC Press, Boca Raton, 1993), pp. 1–499.
- <sup>20</sup>D. Savery and G. Cloutier, "Effects of red blood cell clustering and anisotropy on ultrasound blood backscatter: A Monte Carlo study," *IEEE Trans. Ultrason. Ferroelectr. Freq. Control* **52**, 94–103 (2005).
- <sup>21</sup>R. M. Vlad, R. K. Saha, N. M. Alajez, S. Ranieri, G. J. Czarnot, and M. C. Kolios, "An increase in cellular size variance contributes to the increase in ultrasound backscatter during cell death," *Ultrasound Med. Biol.* **36**(9), 1546–1558 (2010).
- <sup>22</sup>K. K. Shung, Y. W. Yuan, D. Y. Fei, and J. M. Tarbell, "Effect of flow disturbance on ultrasonic backscatter from blood," *J. Acoust. Soc. Am.* **75**, 1265–1272 (1984).
- <sup>23</sup>E. L. Hinrichsen, J. Feder, and T. Jøssang, "Random packing of disks in two dimensions," *Phys. Rev. A* **41**, 4199–4209 (1990).
- <sup>24</sup>J. C. Lagarias, J. A. Reeds, M. H. Wright, and P. E. Wright, "Convergence properties of the Nelder-Mead simplex method in low dimensions," *SIAMJ. Optim.* **9**(1), 112–147 (1998).
- <sup>25</sup>R. K. Saha and G. Cloutier, "Monte Carlo study on ultrasound backscattering by three-dimensional distributions of red blood cells," *Phys. Rev. E* **78**(6), 061919 (2008).
- <sup>26</sup><http://mathworld.wolfram.com/CirclePacking.html> (Last viewed July, 2010).
- <sup>27</sup>H. F. Zhang, K. Maslov, M. Sivaramakrishnan, G. Stoica, and L. V. Wang, "Imaging of hemoglobin oxygen saturation variations in single vessels *in vivo* using photoacoustic microscopy," *Appl. Phys. Lett.* **90**, 053901 (2007).
- <sup>28</sup>A. Seiyama, O. Hazeki, and M. Tamura, "Noninvasive quantitative analysis of blood oxygenation in rat skeletal muscle," *J. Biochem. (Tokyo)* **103**, 419–424 (1988).
- <sup>29</sup>P. M. Shankar, "Ultrasonic tissue characterization using a generalized Nakagami model," *IEEE Trans. Ultrason. Ferroelectr. Freq. Control* **48**, 1716–1720 (2001).
- <sup>30</sup>A. S. Tunis, G. J. Czarnota, A. Giles, M. D. Sherar, J. W. Hunt, and M. C. Kolios, "Monitoring structural changes in cells with high frequency ultrasound signal statistics," *Ultrasound Med. Biol.* **31**, 1041–1049 (2005).
- <sup>31</sup>D. P. Hruska and M. L. Oelze, "Improved parameter estimates based on the homodyned K distribution," *IEEE Trans. Ultrason. Ferroelectr. Freq. Control* **56**, 2471–2481 (2009).
- <sup>32</sup>F. Destrempes and G. Cloutier, "A critical review and uniformized representation of statistical distributions modeling the ultrasound echo envelope," *Ultrasound Med. Biol.* **36**, 1037–1051 (2010).